PHYSICAL REVIEW C, VOLUME 61, 054614

Distribution of compound-nucleus shapes and its influence on evaporation

R. J. Charity
Department of Chemistry, Washington University, St. Louis, Missouri 63130

(Received 10 November 1999; published 20 April 2000)

The tail of the equilibrium distribution of compound-nucleus shapes is shown to extend out to very deformed shapes even for a moderate excitation energy of 100 MeV. The standard Hauser-Feshbach formalism is extended to predict the decay of a deformed compound nucleus as a function of spin, spin projection, and excitation energy. The inclusion of the equilibrium distributions of shapes is found to have little effect on the predicted neutron and proton kinetic energy spectra, but for α particles, the low-energy ''sub-barrier'' region of the spectrum is enhanced, in agreement with experimental data. Langevin simulations, using dissipation given by the wall formula, predict that compound nuclei start evaporating before the shape distribution equilibrates for excitation energies above $\sim$100 MeV.

PACS number(s): 25.70.Gh, 24.60.Dr

I. INTRODUCTION

The evaporation of light particles from excited compound nuclei is a well known decay process for excitation energies above the neutron separation energy. A number of statistical-model computer codes are available, based on either the Weisskopf formalism [1] valid for low spin or the Hauser-Feshbach formalism [2] valid for all spins, to follow the decay of compound nuclei (produced in either fusion, deep inelastic, or other reaction mechanisms) by a cascade of evaporated light particles. These codes are widely used in many areas of nuclear research to predict information about the evaporation residues and the multiplicity, energy, and angular distributions of the evaporated particles. One outstanding problem in the use of evaporation codes is that standard statistical-model calculations are unable to reproduce the large number of ''sub-barrier'' or low-energy α particles emitted in heavy-ion induced fusion reactions. Numerous experimental studies [3–12] have found that the predicted peak in the α-particle kinetic-energy spectrum occurs at a larger energy than observed. Suggested explanations of this observation involve either the reduction of the barrier for α-particle emission or other sources of low-energy α particles. Charity *et al.* [11] considered the emission of unstable clusters, such as ^{5}He fragments, which sequentially decay giving rise to α particles whose kinetic-energy spectrum extends down lower in energy than the corresponding spectrum for directly emitted particles. Subsequent investigations for $E^{*}\sim300$ MeV ^{160}Yb compound nuclei [13] revealed that although this source does exist, its contribution to the total α-particle spectrum is too small to cause any significant change in the predicted peak energy. However, this extra source is responsible for a significant enhancement in the extreme ''sub-barrier'' region.

The barrier for charged-particle emission is a combination of the Coulomb barrier and a centrifugal barrier. In the statistical model, evaporation is generally associated with low centrifugal barriers, except when the level density has a very strong spin dependence, which occurs when the rotational energy increases steeply with angular momentum. This spin dependence favors decays for which the orbital angular momentum of the evaporated particle reduces the spin of the compound nucleus. If the rotational energy's spin dependence is particularly steep, this mechanism leads to the emission of α particles with large orbital angular momenta and hence with significant centrifugal barriers. This situation occurs for the decay of light compound nuclei at high angular momentum where one can often obtain good fits to the experimental kinetic-energy spectra by modifications to the spin dependence of the rotational energy [14–16].

However, for heavier compound nuclei, modifications to the rotational energy have a much smaller effect as these systems have larger moments of inertia, i.e., the rotational energy increases more slowly with spin. In addition, for kinetic-energy spectra gated on evaporation residues [7,10–12] for which fission competition restricts the compound-nucleus spin to moderate values, the magnitude of the centrifugal barrier is already small and any attempt at fitting such data requires a modification of the Coulomb barrier. In principle, reduced Coulomb barriers can be a result of reduced nuclear density [7] or an increase in the surface diffuseness [17], however the most common approach to fitting experimental kinetic-energy spectra is to include into statistical-model calculations distributions of Coulomb barriers associated with a fixed deformation of the compound nucleus [3,5,6,10,12]. Emissions associated with the lower Coulomb barriers populate the low-energy ''sub-barrier'' region, which lies below the peak in the kinetic-energy spectrum. If deformation is the correct explanation of the experimental data, it is important to understand the mechanism responsible for deforming the compound systems. This deformation may be a consequence of the fusion dynamics and evaporation might occur before the compound-nucleus shape relaxes to its equilibrium value [12,18,19] or the deformation may be an intrinsic property of the compound nucleus. It is the latter explanation which will be pursued in the work. Thermally induced shape fluctuations will give rise to an equilibrium distribution of compound-nucleus shapes which depend on the potential-energy surface and the excitation energy. Such shape fluctuations would seem to be an important ingredient in understanding the width of the giant dipole resonance in hot nuclei [20,21]. Before other effects such as dynamics are invoked as the explanation, it is important to determine the equilibrium-shape distribution and its effect on

0556-2813/2000/61(5)/054614(17)/$15.00

the energy spectra of evaporated particles and whether this distribution can be attained before particles are evaporated. In this paper, a start to answering these questions will be made taking into account only spheroidal shapes. Charged-particle emission will be considered only in the framework of the Hauser-Feshbach formalism. In the alternative transition-state formalism, the polarizing effect of the nascent charged particle determines the shape of the residual nucleus at the conditional saddle-point lowering of the Coulomb barrier compared to emission from a spherical system [22]. Also, fluctuations around this conditional saddle-point configuration give rise to a distribution of Coulomb barriers which similarly influence the kinetic-energy spectrum [23].

The following section will be devoted to a theoretical description of the shape distributions. Section III will describe the formalism used to calculate the statistical decay from deformed systems. Examples of the predicted kinetic-energy spectra are given in Sec. IV. Section V is devoted to a discussion of Langevin simulations used to predict the excitation energy at which the shape distribution will equilibrate before evaporation commences. Statistical-model calculations are compared to experimental data in Sec. VI and the conclusions of this work are contained in Sec. VII.

II. SHAPE DISTRIBUTIONS

For spheroidal shapes, the deformation parameter will be taken as the relative quadrupole moment Q related to the radii, $r_\parallel$ and $r_\perp$, perpendicular and parallel to the symmetry axis by [24]

$$Q=\frac{8}{15}\pi\frac{(r_\parallel^2-r_\perp^2)}{r_0^2}, \tag{1}$$

where r_0 is the radius of the sphere with equivalent volume. The relative quadrupole moment is positive for prolate and negative for oblate deformations. The equilibrium distributions of Q and K, the projection of the system's spin J on the symmetry axis, for compound nuclei of excitation energy E^* is

$$\rho^{**}(E^*,J,Q)dQ=\frac{1}{2}\sum_{K=-J}^{J}\rho^*(E^*,J,K,Q)dQ, \tag{2}$$

$$\rho^*(E^*,J,K,Q)dQ=\int\rho_{\mathrm{int}}^*(U,K,Q)\frac{dQdP_Q}{h}, \tag{3}$$

where the intrinsic excitation energy is

$$U=E^*-V(Q)-E^k(P_Q,Q)-E^{\mathrm{crot}}(J,K,Q). \tag{4}$$

The factor of $\frac{1}{2}$ in Eq. (2) results from symmetry considerations [25]. In these equations, P_Q is the canonical conjugate momentum to Q, and the K dependence of the intrinsic level density is [25]

$$\rho_{\mathrm{int}}^*(U,K,Q)=\sqrt{\frac{\hbar^2}{2\pi\mathcal{I}_K(Q)}\frac{a}{U}}\rho_{\mathrm{int}}\left(U-\frac{K^2\hbar^2}{2\mathcal{I}_K(Q)}\right). \tag{5}$$

The quantities V and E^k are the potential energy of deformation and the kinetic energy associated with changes in deformation, respectively. The collective rotational energy is

$$E^{\mathrm{crot}}(J,K,Q)=\frac{[J(J+1)-K^2]\hbar^2}{2\mathcal{I}_\perp(Q)}, \tag{6}$$

where $\mathcal{I}_\perp$ is the moment of inertia of the spheroid perpendicular to its symmetry axis and, for independent particle motion, $\mathcal{I}_K$ is the rigid body moment of inertia parallel to the symmetry axis. The quantity a is the level-density parameter.

For hot nuclei, shell effects are assumed to be washed out and hence liquid-drop deformation energies will be used. The liquid-drop deformation energy can be expressed in the following form [26]:

$$V(Q)=[B_s(Q)-1]E_s^0+[B_c(Q)-1]E_c^0, \tag{7}$$

where E_s^0 and E_c^0 are the surface and Coulomb energies for a spherical nucleus and B_s and B_c express the surface and Coulomb energies of a deformed nucleus in units of the respective spherical quantity. Myers and Swiatecki [27,28] determined the spherical energies from fitting ground-state masses as

$$E_s^0=17.9439\left[1-1.7826\left(\frac{N-Z}{A}\right)^2\right]A^{2/3}\ \mathrm{MeV}, \tag{8}$$

$$E_c^0=0.7053\frac{Z^2}{A^{1/3}}\ \mathrm{MeV}. \tag{9}$$

The functions B_s and B_c have been determined for spheroidal deformations by Beringer and Knox [29].

The kinetic energy associated with changes in deformation is determined from the associated momentum P_Q and an inertia parameter $m(Q)$:

$$E^k(P_Q,Q)=\frac{(P_Q)^2}{2m(Q)}. \tag{10}$$

When shell effects are washed out, the hydrodynamical inertia from Ref. [24] is appropriate.

To perform the integrals over momentum, is should be remembered that the intrinsic level density is a very rapidly rising function of excitation energy. Thus, only small values of E^k will contribute significantly and it is useful to expand the level density as

$$\rho_{\mathrm{int}}(U-x)=\rho_{\mathrm{int}}(U)\exp\left(-\frac{x}{T}\right), \tag{11}$$

where the nuclear temperature is defined by

$$\frac{1}{T}=\frac{d\ln(\rho_{\mathrm{int}})}{dU}. \tag{12}$$

For a Fermi-gas level density, the temperature can be expressed in terms of the level-density parameter a as T

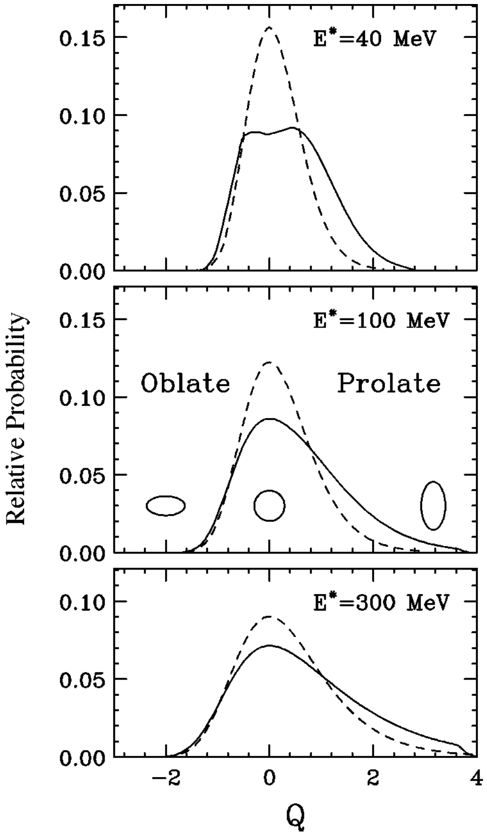

FIG. 1. Predicted probability distributions of the relative quadrupole moment Q for ^{160}Yb compound nuclei at excitation energies of 40, 100, and 300 MeV. The solid curves indicate the results for $J=60\hbar$ while the dashed curves were obtained for $J=0\hbar$. The relative quadrupole moments for spherical and deformed shapes with major and minor axes that differ by a factor of 2 are indicated by the appropriately shaped figures.

$\approx\sqrt{U/a}$. With this approximation, the integration over the momentum coordinate in Eq. (3) yields

$$\rho^*(E^*,J,K,Q)\,dQ=\rho^*_{\rm int}(U',K,Q)\sqrt{\frac{T(Q)m(Q)}{2\pi\hbar^2}}dQ, \tag{13}$$

where the temperature, $T(Q)=\sqrt{U'/a}$, is deformation dependent and now

$$U'=E^*-V(Q)-E^{\rm crot}(J,K,Q). \tag{14}$$

Examples of the predicted shape distributions $\rho^{**}(E^*,J,Q)$ are shown in Fig. 1 for ^{160}Yb compound nuclei at $J=0$ and $60\hbar$ and $E^*=40$, 100, and 300 MeV. The distributions extend over both prolate and oblate shapes. Their width increases as the excitation energy increases. However, their dependence on angular momentum is stronger. For $J=60\hbar$, the distributions extend out to strongly deformed prolate shapes with their tails reaching the ‘‘superdeformed’’ $Q=3.2$ prolate shape (length of axes differ by a factor of 2). For very prolate shapes, the systems will become unstable to the fission degree of freedom and it is useful to try and exclude such fission-unstable configurations. To this end, the condition that the potential-plus-rotational energy be less than the value for the saddle-point configuration was applied, i.e.,

$$V(Q)+E^{\rm rot}(J,K,Q)<E_{\rm sad}(J)+\frac{K^2\hbar^2}{2}\left[\frac{1}{\mathcal{I}_K^{\rm sad}}-\frac{1}{\mathcal{I}_\perp^{\rm sad}}\right], \tag{15}$$

where $E_{\rm sad}$, the energy of the saddle-point configuration and its moments of inertia, $\mathcal{I}_K^{\rm sad}$ and $\mathcal{I}_\perp^{\rm sad}$, are taken from the calculations of Sierk [30].

It has often been assumed in the past that the typical shapes of hot, rotating compound nuclei are well described by the rotating liquid drop model [31] (RLDM), which minimized the sum of the potential and total rotational energies, the latter being the sum of the intrinsic and collective rotational energies:

$$E^{\rm rot}(J,K,Q)=E^{\rm crot}(J,K,Q)+\frac{K^2\hbar^2}{2\mathcal{I}_K(Q)}. \tag{16}$$

The RLDM ground-state configurations are approximately oblate, except for the largest angular momenta, while the predicted distributions in Fig. 1 have somewhat larger yields for prolate deformations. Clearly, the RLDM ground-state configurations are not particularly representative of the overall equilibrium distribution, however their importance becomes more transparent when looking at the predicted joint distributions of Q and K. As an example, ρ^* is displayed as a contour plot in Fig. 2(a) for the $J=60\hbar$, $E^*=100$ MeV ^{160}Yb system. The potential-plus-rotational energy, which is plotted as a function of Q and K in Fig. 2(b), has two minima: one oblate for $K=J$ and one prolate for $K=0$. The oblate minimum at $Q\sim-0.5$ (the lowest of the two, but by only $\sim$1 MeV) corresponds roughly to the RLDM ground-state configuration and is associated with the largest peak in the joint distribution [Fig. 2(a)]. The prolate minimum is only stable because of the restricted shape degrees of freedom (it is unstable to ellipsoidal deformations [32,33]). This prolate minimum is also associated with a peak in the joint distribution and there is a significant yield in the ridge joining the two peaks.

III. DECAY OF DEFORMED SYSTEMS

Given the equilibrium distributions of Q and K predicted in the preceding section, how do they affect the kinetic-energy spectra of evaporated particles? In addressing this question, let us assume that the statistical decay width is independent of P_Q. Further assume that Q remains unchanged during the evaporation process, i.e., both the parent and daughter have the same deformation. For any single compound nucleus, thermal shape fluctuations will give rise to changes in the decay width as the shape evolves with time, however for an equilibrium ensemble, the population and decay rate from a particular deformation will both be constant.

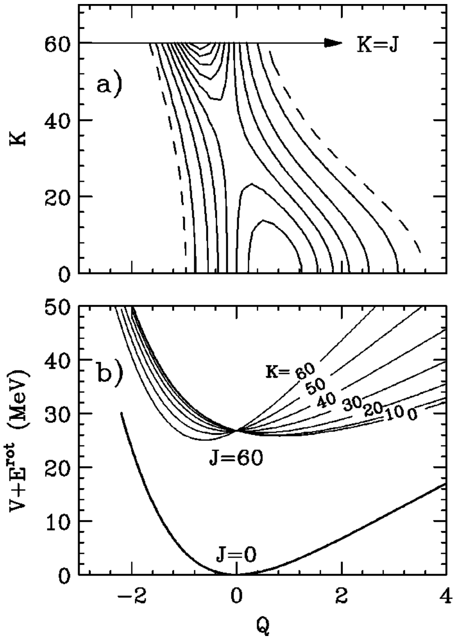

FIG. 2. (a) Predicted joint distribution ρ^* of relative quadrupole moment Q and spin projection K obtained for $J=60\hbar$, $E^*=100$ MeV ^{160}Yb compound nuclei. The contour interval for the solid contours is 10% of the maximum value of ρ^* and the dashed contour represents 5% of this maximum. (b) The predicted dependence of the potential-plus-rotational (intrinsic + collective) energy for the same system with $J=0$ and $60\,\hbar$ for selected values of K.

A. Statistical formalism

Statistical decay widths are typically calculated for compound systems with significant spin using the Hauser-Feshbach formalism [2]. A number of studies have incorporated deformation effects into this formalism. Modifications associated with transmission coefficients [3,8,16,34–36], deformed rotational energies [3,8,16,35], collective enhancement of level densities [37,38], and deformation-dependent separation energies [39] have been considered. However, none of these modifications allow one to calculate the decay from a particular K state. To permit this, the Hauser-Feshbach formalism has been extended by including the explicit summations over the projections of the angular momenta of the emitted particle and the daughter nucleus via Clebsch-Gordan coefficients $(j_1,\, m_1,\, j_2,\, m_2|j,m)$, i.e., the modified decay width is

$$\begin{aligned}\Gamma = {} & \frac{1}{2\pi\rho^*(E^*,J_p,K_p,Q)}\\ & \times\int d\epsilon \sum_{J_d=0}^{\infty}\sum_{K_d=-J_d}^{J_d}\sum_{j=|J_p-J_d|}^{J_p+J_d}\sum_{l=|j-s|}^{j+s}\sum_{m=-l}^{l}\\ & \times(l,m,s,K_p-K_d-m|j,K_p-K_d)^2\\ & \times(J_d,K_d,j,K_p-K_d|J_p,K_p)^2\\ & \times T_{l,m}(\epsilon,Q)\rho^*(E^*-E^0_{\rm sep}-\epsilon,J_d,K_d,Q), \qquad (17)\end{aligned}$$

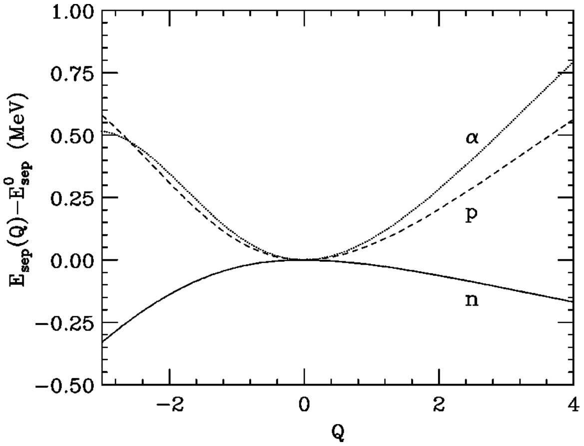

FIG. 3. Predicted deformation dependence of the separation energies for removing a neutron, a proton, and an α particle from ^{160}Yb.

where the subscripts d and p refer to the daughter and parent nucleus, respectively. The quantities s, l, and j are the spin, orbital, and total angular momentum of the particle evaporated with kinetic energy ϵ and $E^0_{\rm sep}$ is the separation energy for the removal of this particle. The transmission coefficients are averages over the surface of the nucleus and are now dependent on m, the projection of l on the symmetry axis (see Sec. III B). The thermal excitation energy of the daughter is

$$U_d = E^* - V_d(Q) - E_d^{\rm crot}(J,K,Q) - E^0_{\rm sep} - \epsilon. \qquad (18)$$

Note that the deformation energy of the daughter $V_d(Q)$ is different from that of the parent $V_p(Q)$. The difference between these has been combined by Lestone *et al.* [39] together with the separation energy to give a so-called deformation-dependent separation energy:

$$E_{\rm sep}(Q) = E^0_{\rm sep} + V_p(Q) - V_d(Q) \qquad (19)$$

$$= E^0_{\rm sep} + [B_s(Q)-1][(E^0_s)_p - (E^0_s)_d] \qquad (20)$$

$$+ [B_c(Q)-1][(E^0_c)_p - (E^0_c)_d]. \qquad (21)$$

The effects associated with a deformation-dependent separation energy are already implicitly considered in Eq. (17) and $E_{\rm sep}(Q)$ should not explicitly appear is this equation. The deformation dependence of the separation energy is plotted for neutron, proton, and α-particle removal from a ^{160}Yb system in Fig. 3. As found in Ref. [39], the separation energy increases with deformation for charged particles, while it decreases slowly for neutrons.

For a spherical nucleus, the transmission coefficients are independent of m and the level density of the daughter is independent of K_d. The summation of the Clebsch-Gordan coefficients over m and K_d then gives unity and Eq. (17) reduces to the standard Hauser-Feshbach formalism valid for spherical systems.

B. Transmission coefficients

For a deformed nucleus, the transmission coefficients should depend on m. For example, consider a prolate shape where the Coulomb barrier is lowest for emission from its tips and highest for emission at the waist. Classically the orbital angular momentum for emission from the tips must be perpendicular to the symmetry axis, i.e., $m=0$, whereas at the waist, all values of m are possible. One would therefore expect that, after averaging over the surface area, the barrier for $m=0$ emission is lower than for $m=l$ emission, and vice versa for an oblate shape. To estimate the l and m dependence of the transmission coefficients, the equivalent-spheres approximation [16,40] was modified. For each point on the surface of a deformed nucleus, in this approximation, transmission coefficients are calculated for an equivalent spherical system with the same radius r. Each set of spherical transmission coefficients is weighted by the element of surface area ds associated with that point on the nuclear surface and the average is then taken over the whole surface area. The dependence on m is obtained by noting that the orbital angular momentum at each point on the surface is classically perpendicular to the radius vector to that point. Taking this radius vector as a projection axis, we thus assign a quantum projection of $m'=0$ for the orbital angular momentum relative to this axis. To relate the m' state associated with this projection axis to those m states associated with the symmetry axis, one must weight by the square of the quantum-mechanical rotation matrix $r^{l}_{m,m'}(\theta)$ [41], where θ is the angle between the axes. With this extra weighting, and after some simplification, the transmission coefficients reduce to

$$T_{l,m}(\epsilon,Q)=\frac{\oint T_l^{\mathrm{sphere}}(\epsilon,r)\,|P_l^m(\cos\theta)|^2 ds}{\oint |P_l^m(\cos\theta)|^2 ds}, \qquad (22)$$

where P_l^m is the Legendre function. The spherical transmission coefficients $T_l^{\mathrm{sphere}}(\epsilon,r)$ were calculated with the incoming-wave boundary-condition model [42] using real nuclear potentials from global optical-model fits for neutrons [43], protons [44], and α particles [45]. Examples of transmission coefficients calculated with this procedure are shown in Fig. 4 for the $\alpha+$Yb channel. It is clear for $l=10$ that there is a very strong m dependence when the deformation is large. Also it should be stressed that although these transmission coefficients are believed to contain the most important physics, they are only approximate. The averaging of spherical transmission coefficients over the surface area of the nucleus ignores multipole moments of the Coulomb field and the surface-curvature dependence of the nuclear field. Also as the Coulomb and nuclear forces are not central forces for a deformed system, the orbital angular momentum of the emitted particle is not a constant of motion. [A related effect, the rotation of the compound nucleus (for $J\neq 0$) during the emission of the particle, was found in Ref. [46] to be small.] As such, these transmission coefficients should only be used to give approximate information as to the effect of deformation.

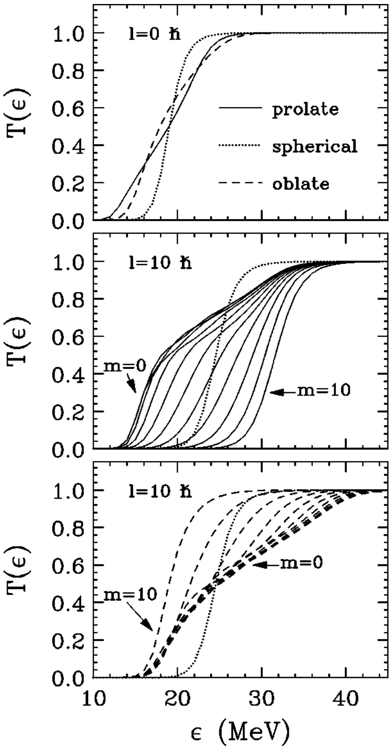

FIG. 4. Transmission coefficients calculated for the $\alpha+$Yb channel with orbital angular momenta of $l=0$ and $10\hbar$. The dotted curves are for a spherical compound system, while the solid and dashed curves were obtained with prolate and oblate deformations, where the major and minor axes differ by a factor of 2.

IV. KINETIC-ENERGY SPECTRA OF EVAPORATED PARTICLES

A. Dependence on Q and K

The new evaporation formalism discussed above has been incorporated into the Monte Carlo, statistical-model computer code GEMINI [47]. In the following, examples of the Q and K dependence of the decay are illustrated for the $E^*=100$ MeV ^{160}Yb compound system with a level-density parameter of $a=A/10$ MeV^{-1}. The Q dependence of the kinetic-energy spectra of first-chance protons, neutrons, and α particles from a $J=0\hbar$ system is shown in Fig. 5. The predictions for a spherical system are given by the dotted curves, while the solid and dashed curves were obtained for highly deformed prolate and oblate shapes, respectively, in both cases the major and minor axes differ by a factor of 2. The largest dependence on deformation is clearly observed for α particles. The peak in their kinetic-energy spectrum moves down to lower energies as the deformation increases, a direct result of the increase in the transmission coefficients at these low kinetic energies (Fig. 4). At the higher kinetic energies where the transmission coefficients approach unity and are thus independent of Q, the emission probabilities are larger for the spherical system. The most important effect now is that the spherical system is hottest (no deformation energy) and for charged particles this is further enhanced because the spherical system also has the smallest separation energies (Fig. 3).

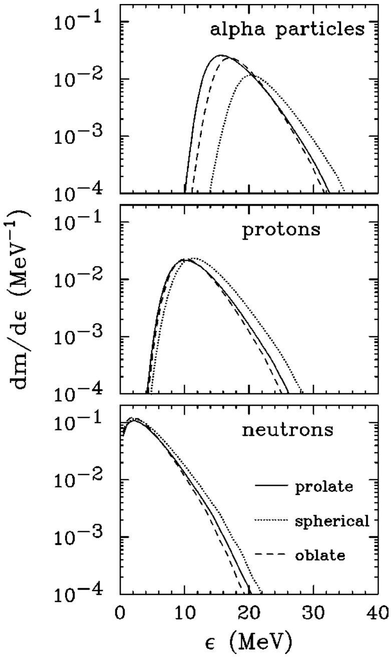

FIG. 5. Predicted kinetic-energy spectra of first-chance neutrons, protons, and α particles evaporated from $E^* = 100$ MeV, $J = 0\hbar$ ^{160}Yb compound systems with three different deformations. The dotted curves are for a spherical compound system, while the solid and dashed curves were obtained with prolate and oblate deformations, where the major and minor axes differ by a factor of 2.

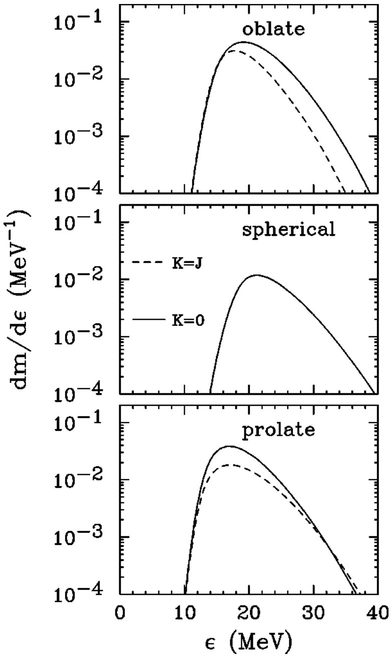

FIG. 6. Predicted first-chance α-particle kinetic-energy spectra for $E^* = 100$ MeV, $J = 60\hbar$ ^{160}Yb compound systems with spherical, prolate, and oblate deformations. The deformed systems have major and minor axes which differ by a factor of 2. Calculations where the initial rotational state is purely collective ($K=0$) or purely intrinsic ($K=J$) are indicated by the solid and dashed curves, respectively.

The dependence of the decay on K is shown for $J = 60\hbar$ in Fig. 6. The peaks in the α-particle kinetic-energy spectra again move down to lower energies as the deformation increases for all values of K. However, the shape of the spectra do show important dependencies on the spin projection. In understanding these differences, we need to expand on the discussion of the spin dependence of the rotational energy mentioned in Sec. I. Although for the ^{160}Yb system this spin dependence is not so large that it leads to a noticeable increase in the peak energy due to large centripetal barriers, it is still responsible for a spin enhancement in the yield of heavy fragments, such as α particles, which can remove significant angular momentum from the decaying system. The magnitude of this spin enhancement depends again on the slope of the rotational energy's spin dependence and also on the transmission coefficients. The rotational energies are plotted in Fig. 7 for the oblate and prolate shapes with $K = 0$ and $K = J$. The slope is largest with $K = 0$ for oblate shapes and with $K = J$ for prolate shapes. Ignoring the effects of the transmission coefficients, one might expect these two configurations to have the largest α-particle yields. However, this is only true for the oblate configuration. Now the compound-nucleus spin is most efficiently removed by an evaporated α particle if $m = 0$ for the $K = 0$ case and $m = l$ for the $K = J$ case. Thus, the extra enhancement for the $K = 0$ oblate case is tempered at low kinetic energies by the reduced transmission coefficients for $m = 0$ (see Fig. 4).

It is important to note that for the oblate case, the transmission coefficients, for all m values, are non-negligible down to low kinetic energies, although their relative magnitude may be quite different. For prolate deformations, on the other hand, this is not the case. The transmission coefficients for $m = l$ are only significant at high kinetic energies (see Fig. 4). This fact is very important for the $K = J$ prolate configuration which has the largest J dependence of the rotational energy (Fig. 7). The expected spin enhancement is not observed at low and medium kinetic energies as the

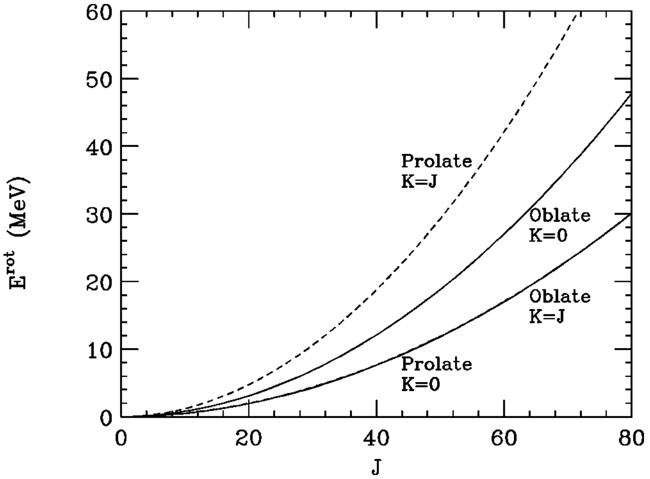

FIG. 7. Spin dependence of the total rotational energy (collective plus intrinsic) for the oblate and prolate shapes used in the calculations shown in Fig. 6. Curves are shown for both $K = 0$ (solid) and $K = J$ (dashed). However, the prolate $K = 0$ and the oblate $K = J$ curves overlap.

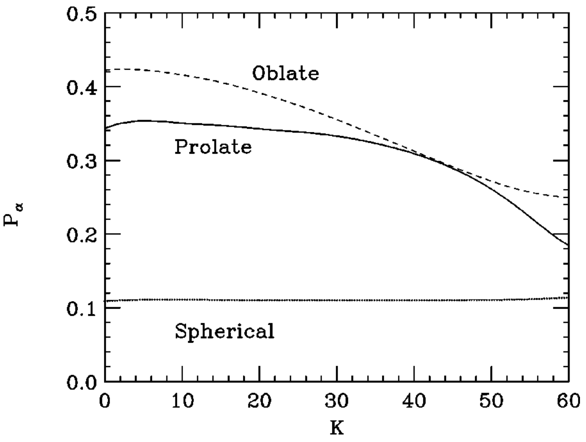

FIG. 8. Predicted first-chance α-particle emission probability for $E^*=100$ MeV ^{160}Yb compound nuclei at $J=60\hbar$. Curves are shown giving the K dependence of the probability for prolate, oblate, and spherical deformations. The oblate and prolate deformations have major and minor axes which differ by a factor of 2.

transmission coefficient for high m values are almost zero and prevent the removal of significant angular momentum by α-particle emission. It is only at the highest kinetic energies that a significant spin enhancement is achieved and the yield for $K=J$ becomes larger than the $K=0$ prolate prediction. The larger ''temperature'' which characterizes the slope of the high-energy tail of the kinetic-energy spectrum for the $K=J$ prolate case is thus explained as a progressive increase of the spin enhancement with kinetic energy and is not a consequence of the initial temperature of the compound nucleus. In fact, the initial temperature for this configuration is the smallest of all the examples in Fig. 6 as its potential-plus-rotational energy is largest.

The dependence of the energy-integrated first-chance α-particle emission probability on K is shown in Fig. 8. The α-particle probability is clearly enhanced by deformation no matter what the value of K is. Oblate collective rotations ($K=0$) are responsible for the greatest enhancements while prolate intrinsic rotations ($K=J$) have the lowest enhancements. However, these two configurations are not well represented in the equilibrium Q-K distributions (Sec. II).

B. Averages over *Q* and *K* distributions

First-chance kinetic-energy spectra, averaged over the equilibrium distributions of Q and K, are shown for the $E^*=100$ MeV ^{160}Yb system in Fig. 9 (solid curves). For comparison, the dashed curves show the results of more standard statistical-model calculations using only spherical transmission coefficients and rotational energies from the calculations of Sierk [30]. For $J=0\hbar$ systems, the effect of averaging over the equilibrium distribution is not large, the only significant change being a small enhancement for ''sub-barrier'' α particles. For the higher compound-nucleus spin, this enhancement is much larger and the peak position occurs at an energy ~2 MeV lower in value compared to the standard calculation. The reasons for the large spin dependence of this enhancement can be inferred from Fig. 10, where the equilibrium Q-K distribution [Fig. 10(a)] is compared to the

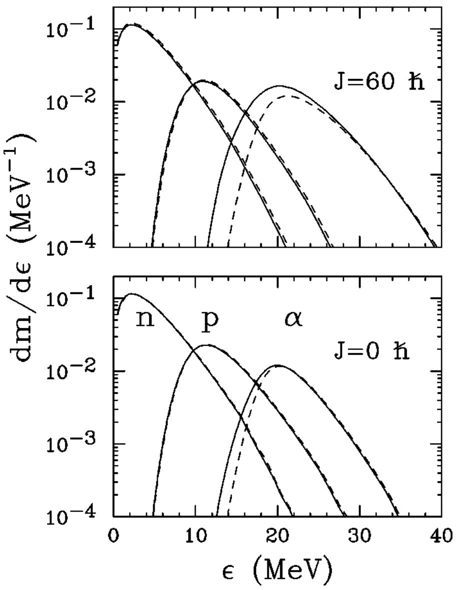

FIG. 9. Predicted kinetic-energy spectra for first-chance evaporation of neutrons, protons, and α particles from $E^*=100$ MeV ^{160}Yb compound nuclei with spins of 0 and 60$\hbar$. The solid curves were obtained from the predicted equilibrium distributions of Q and K, while the dashed curves are from a more standard calculation with spherical transmission coefficients.

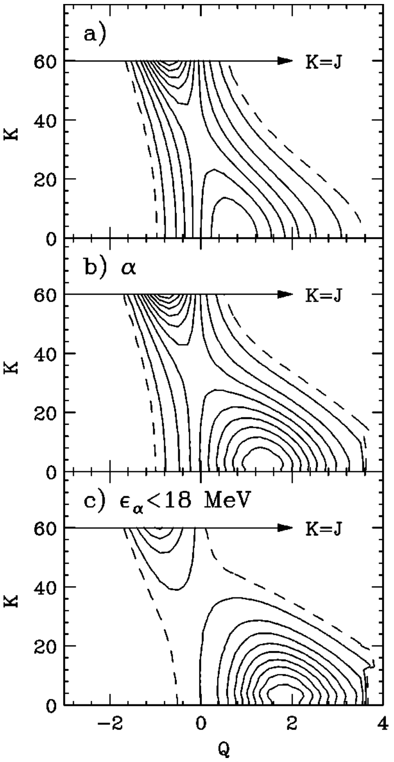

FIG. 10. Predicted joint distributions of Q and K for $E^*=100$ MeV, $J=60\hbar$ ^{160}Yb compound nuclei. (a) Equilibrium distribution. (b) The same distribution, but also with the requirement that the system decays by α emission. (c) With the extra requirement that the system decays by the emission of a low-energy α particle ($\epsilon_\alpha<18$ MeV).

same distribution with the extra condition that an α particle was emitted [Fig. 10(b)], and where this α particle has a low kinetic energy, $\epsilon_\alpha < 18$ MeV [Fig. 10(c)]. Both Figs. 10(b) and 10(c) show an increase in the relative number of highly deformed prolate systems. The enhancement of low-energy α particles is thus largely attributed to these highly-deformed prolate systems which become more probable at larger compound-nucleus spins (see Sec. II). Figure 10(c) suggests that the detection of a low-energy α particle could be used to experimentally select out highly deformed prolate systems. However, it is not clear whether this deformation will be preserved at subsequent decay steps (Sec. V).

Further enhancements of the sub-barrier α particles are possible if a surface-area dependence of the level-density parameter is assumed. This increases the relative probability of highly deformed shapes, which have larger surface areas. Calculations were performed using the level-density parameter of Ignatyuk *et al.* [48], however the extra sub-barrier enhancement was quite modest. Given the other uncertainties in calculating the sub-barrier enhancement, it was decided not to pursue this effect in the present work.

V. LANGEVIN SIMULATIONS

An important consideration before comparing predicted spectra to data is whether the time required for the equilibrium distribution to develop is shorter than the typical time for evaporation. If this is not the case, evaporation will, on average, occur before the equilibrium distribution is established. There are three time scales to consider; first the evaporation time τ_{ev}; next the time required for the build up of shape fluctuations; and finally the dynamical time associated with the fusion reaction. As an example of the latter, consider the fusion reaction of $^{64}\text{Ni}+{}^{96}\text{Mo}$. The evolution of shapes leading to a fused system can be followed with the code HICOL [49] which calculates the dissipation of energy with the wall-plus-window formula of Ref. [50]. The window formula is valid early in the collision when there is still a ‘‘neck’’ connecting the targetlike and projectilelike fragments and involves the transfer of nucleons between these fragments. In the wall formula, dissipation is mediated through interactions of the moving walls of the nucleus with the nucleons striking it; the rate of energy loss is given by [50]

$$\frac{dE_{\text{diss}}}{dt} = \frac{3}{4}\rho_m v_f \oint v_n^2 ds, \tag{23}$$

where ρ_m is the mass density, v_f is the Fermi velocity, and v_n is the normal velocity of the surface.

The results of the fusion simulation performed with HICOL for a bombarding energy of $E/A = 5$ MeV and with zero impact parameter are shown in Fig. 11 as the temporal evolution of Q and the dissipated thermal excitation energy U. In this calculation, there is an extremely short period of less than 0.5 zs when most of the energy is dissipated, after which a deformed mononuclear configuration is formed with deformation Q_{HICOL}. Subsequently, the quadrupole moment slowly diminishes as the shape evolves towards sphericity. Within our spheroidal approximation, the dynamics of this latter motion can also be followed. The equation of motion is

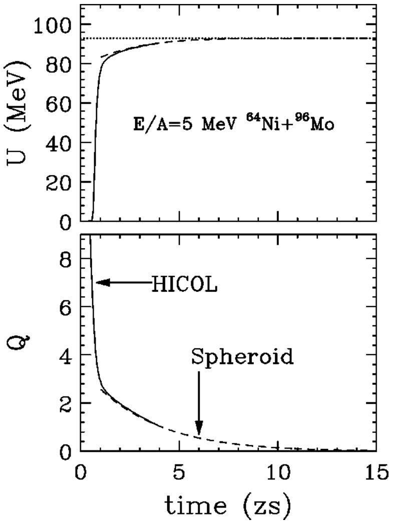

FIG. 11. Predicted time evolution of the relative quadrupole moment Q and dissipated energy U for the $E/A = 5$ MeV $^{64}\text{Ni}+{}^{96}\text{Mo}$ reaction at zero impact parameter. The solid curves were obtained from the HICOL code and the dashed curves from a spheroidal approximation (see text).

$$m(Q)\ddot{Q} = -\frac{1}{2}\frac{dm}{dQ}(\dot{Q})^2 - \frac{dV}{dQ} - \eta(Q)\dot{Q}, \tag{24}$$

where the friction coefficient $\eta(Q)$ is determined from the wall formula [Eq. (23)] [24]:

$$\frac{dE_{\text{diss}}}{dt} = \eta(Q)(\dot{Q})^2. \tag{25}$$

The friction predicted by the wall formula is very large and the rate of change of the deformation rapidly reaches its ‘‘terminal velocity’’:

$$\dot{Q} = \frac{-\dfrac{dV}{dQ}}{\eta(Q)}. \tag{26}$$

The dashed curves in Fig. 11 show the predictions of the above equation using as an initial deformation the value predicted by the HICOL code after the rapid-dissipation period Q_{HICOL}. The results of this spheroidal approximation and of the HICOL simulations are in excellent agreement and Q decays approximately exponentially with a time constant of 3.2 zs.

Next consider the time scale for the build up of fluctuations which are ignored in Eq. (24) and the HICOL simulations. If we make the most simplistic assumptions that the motion is Markovian and use the Einstein equation (relating the magnitude of the fluctuations and dissipation), the motion can be described with the following Langevin equation:

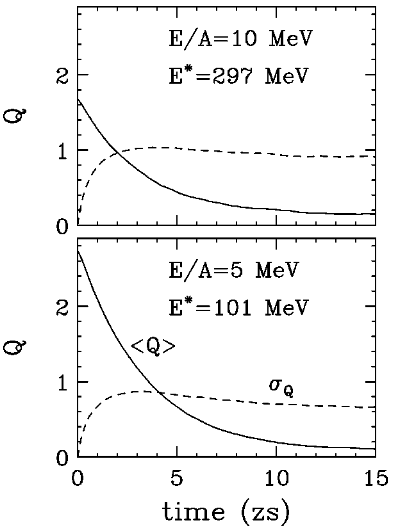

FIG. 12. Predicted time evolution of the mean (solid curves) and standard deviation (dashed curves) of the relative quadrupole moment Q distribution for the $E/A=5$ and 10 MeV $^{64}\mathrm{Ni}+^{96}\mathrm{Mo}$ reactions at zero impact parameter.

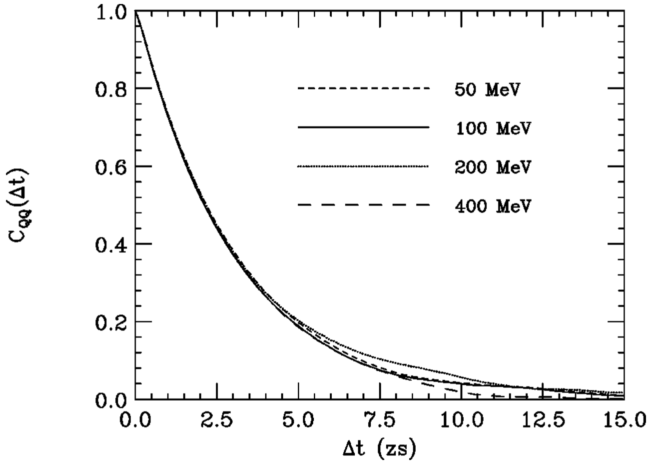

FIG. 13. Predicted dependence of the two-time Q correlation function plotted as a function of the interval Δt between the two times. The results were obtained for $J=0\hbar$ $^{160}\mathrm{Yb}$ systems at the four indicated excitation energies.

$$m(Q)\ddot{Q}=-\frac{1}{2}\frac{dm}{dQ}(\dot{Q})^2-\frac{dV}{dQ}-\eta(Q)\dot{Q}-\sqrt{T(Q)\,\eta(Q)}\,\xi(t). \tag{27}$$

The last term is associated with a fluctuating force where $\langle\xi(t)\rangle=0$ and $\langle\xi(t)\xi(t')\rangle=2\delta(t-t')$. It is assumed that the initial period of rapid dissipation is too short a time for significant fluctuations to develop and hence all Langevin simulations were started with the same deformation Q_{HICOL}. After performing many simulations, the evolution of $\langle Q(t)\rangle$ and $\sigma_Q(t)$, the mean and standard deviation of the Q distributions, is calculated. Examples are shown for $E/A=5$ and 10 MeV $^{64}\mathrm{Ni}+^{96}\mathrm{Mo}$ reactions (zero impact parameter) in Fig. 12. In this figure, note that the initial deformation Q_{HICOL} decreases at higher bombarding energies. Also in both examples, the fluctuations build up very quickly (within a couple of zs) after which the standard deviation is very close to its equilibrium value. The limiting time is therefore not the time required to build up the fluctuations, but the dynamical time required to bring the mean deformation to its equilibrium value. A dynamical time τ_{dyn} will be defined as the time required to bring the mean deformation to within $\sigma_Q(\infty)/2$ of the equilibrium value, i.e.,

$$\langle Q(\tau_{\mathrm{dyn}})\rangle-\langle Q(\infty)\rangle=\frac{\sigma_Q(\infty)}{2}. \tag{28}$$

This dynamical time is reaction dependent and for the example reaction it decreases with bombarding energy due to the decreasing value of Q_{HICOL}. For very asymmetric entrance channels, the initial deformation will be much smaller and the time required to equilibrate the shape degrees of freedom will be limited by the fluctuations. Another related time is that required for systems to ''forget'' their deformation. This is of interest if one is looking for correlations in deformations between different evaporation steps once the equilibrium distribution is attained. To investigate this, it is useful to look at the two-time correlation function,

$$C_{QQ}(t,t')=\frac{\sigma_{QQ'}}{\sigma_Q^2}, \tag{29}$$

where Q and Q' are the deformations at the two times t and t', respectively. The correlation function was determined from a Langevin simulation averaging over all times ($\geqslant\tau_{\mathrm{dyn}}$) and is plotted as a function of $\Delta t=|t-t'|$ in Fig. 13. The correlation function is almost independent of excitation energy, a result which is due to the cancellation of two effects; diffusion is faster at higher temperatures, but the width of the equilibrium distribution also increases. As correlations decrease approximately exponentially with time, the time constant τ_c of this decay will serve as a measure of the correlation time (3.0 zs in these simulations).

The time scales τ_{dyn} and τ_c are plotted as a function of excitation energy in Fig. 14(a) and compared to the evaporative time scale $\tau_{\mathrm{ev}}=\hbar/\Gamma_{\mathrm{tot}}$ (Γ_{tot} is the total decay width). The solid and dashed curves were calculated for level-density parameters of $A/10$ and $A/8$ MeV^{-1}, respectively. The evaporative time scales change very rapidly with excitation energy and, compared to this, the difference between τ_{dyn} and τ_c is not very important. For $E^*>100$ MeV, $\tau_{\mathrm{ev}}\ll\tau_{\mathrm{dyn}}$, τ_c and significant evaporation will occur before the equilibrium distribution becomes established. As the correlation time also serves as an estimate of τ_{dyn}, let us use the excitation energy E_c^* for which $\tau_{ev}=\tau_c$ as an indication of the point at which evaporation occurs before the collective degrees of freedom are equilibrated. This quantity is plotted in Fig. 15 as a function of mass number for two level-density parameters ($A/8$ and $A/10$ MeV^{-1}). No major dependence on compound-nucleus mass is seen. For symmetric entrance channels, this excitation energy will be slightly smaller as $\tau_{\mathrm{dyn}}>\tau_c$.

So far shape fluctuations have only been discussed for systems with zero spin. For finite angular momentum, one

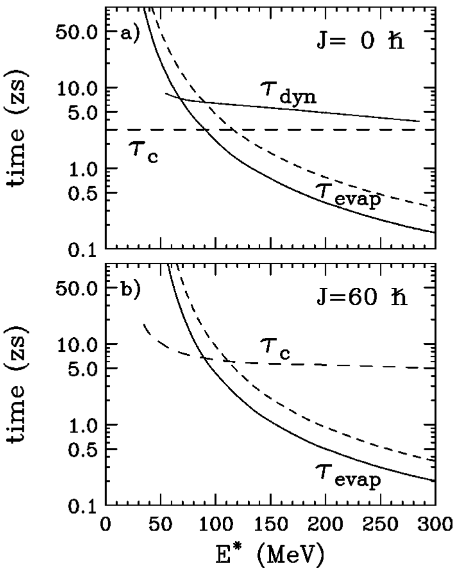

FIG. 14. Comparison of the dynamical time $\tau_{\rm dyn}$, the correlation time τ_c, and the evaporation time $\tau_{\rm ev}$ for the ^{160}Yb system at spins of 0 and 60 $\hbar$. The evaporation times, calculated with level-density parameters of $A/10$ and $A/8$ MeV^{-1}, are indicated by the solid and short-dashed curves, respectively.

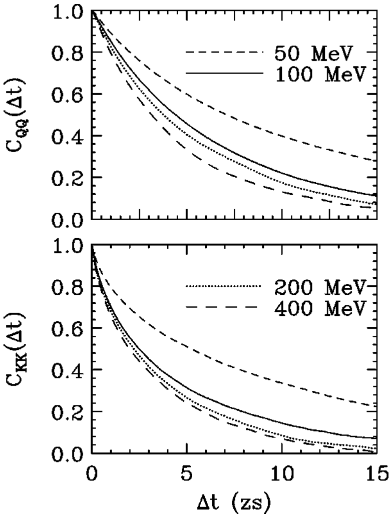

FIG. 16. Predicted Q and K two-time correlation functions are plotted as a function of the interval Δt between the two times. The results were obtained for $J=60\hbar$ ^{160}Yb systems at the four indicated excitation energies.

must also consider fluctuations in *K*. Unfortunately, the magnitude of *K* fluctuations is not well known. When calculating fission-fragment angular distributions it is usually assumed that the equilibrium *K* distribution is achieved for the saddle-point configuration, but subsequently *K* remains frozen during the descent from the saddle to the scission point. This dichotomy between *K* relaxation as one crosses the saddle point must be a consequence of either different time scales of the motion on either side of the saddle point or a decrease in the *K* relaxation rate with deformation. Close to sphericity, the symmetry axis and *K* become less well defined leading to a rapid randomization of *K*. Thus a deformation dependence of the *K* relaxation rate is expected. Even if *K* remains frozen for any appreciable deformation, the rapid relaxation of *K* at sphericity may be the controlling factor for the total equilibrium time scale. To illustrate this, Langevin simulations were performed where *K* remains fixed, except when *Q* passes through zero, at which point the value of *K* is randomized. The corresponding two-time correlation functions for *Q* and *K* obtained for $J=60\hbar$ ^{160}Yb systems are presented in Fig. 16. Unlike the $J=0\hbar$ result (Fig. 13), the correlation function now depends on excitation energy. The *Q* and *K* correlation functions have similar, but not identical, behavior for a particular excitation energy, but the correlation time of both decreases slowly with increasing excitation energy. This correlation time τ_c is compared to the evaporation time scale in Fig. 14(b). One should note that this value of τ_c is a maximum value; if there are significant *K* fluctuations at large deformation, then the actual value will be smaller. However, it cannot be significantly smaller as the time scale is limited by the *Q* fluctuations and thus the time scale should be larger than the value of τ_c for $J=0\hbar$ [Fig. 14(a)]. The excitation energy E_c^* where collective nonequilibrium effects first become important is again $\sim$100 MeV even if there is significant *K* relaxation at large deformations. Values of E_c^* determined for ^{160}Yb and ^{100}Rh systems as a function of spin are plotted in Fig. 17. This figure also indicates that E_c^* is approximately 100 MeV with no great dependence of compound-nucleus mass or spin except for spins around $55\hbar$ in the ^{100}Rh system where E_c^* suddenly drops in value and approaches the yrast line. In fact, for spins above $55\hbar$, there is no excitation energy region where the evaporation time scale is larger than the correlation time in the ^{100}Rh system. The reason for this behavior can be understood from Fig. 18, which shows the predicted *Q*-*K* equilibrium distribution for the $J=55\hbar$, $E^*=100$ MeV ^{100}Rh system. The peaks in the distribution for prolate and oblate shapes observed in Fig. 2(a) are still present, but the ridge connecting them is con-

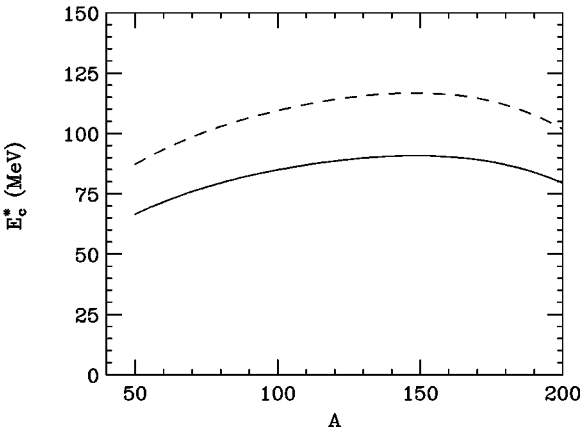

FIG. 15. The predicted excitation energy in the Langevin simulations where the time scale for the thermalization of the shape degree of freedom is equal to the evaporative time scale. The results, plotted against the compound-nucleus mass, were obtained with level-density parameters of $A/10$ (solid curve) and $A/8$ MeV^{-1} (dashed curve).

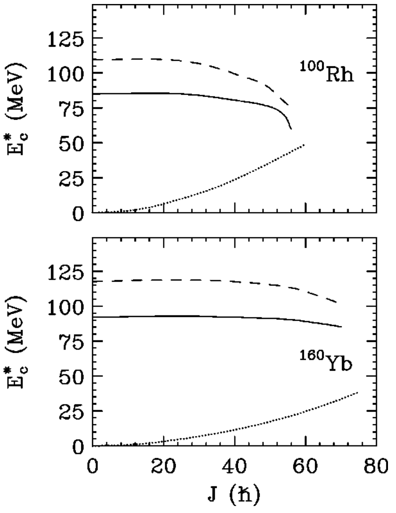

FIG. 17. Predicted critical excitation energy at which the collective correlation times τ_c and the evaporation times τ_{ev} are equal is plotted as a function of compound-nucleus spin for the ^{100}Rh and ^{160}Yb systems. The results obtained with level-density parameters of $A/10$ and $A/8$ MeV^{-1} are indicated by the solid and dashed curves, respectively. For comparison, the yrast lines predicted in the calculations of Sierk [30] are indicated by the dotted lines.

siderably diminished. This narrow connecting region between these two main parts of the distribution represents a ''bottleneck'' which retards the onset of equilibrium between the oblate and prolate regions. To diffuse across this bottleneck one must overcome the ~4 MeV barrier separating them at $J=55\hbar$. This barrier also increases with increasing spin. The other important barrier, the fission barrier, which retards the prolate group from fissioning is 11 MeV at $55\hbar$ [30] and so escape across this barrier is less probable and evaporation would still be the dominant decay mode up to spins of $59\hbar$, where the neutron separation energy and the fission barrier are equal. In the narrow angular-momentum region, 55–59 $\hbar$, the above calculations would suggest that evaporation would be mostly from the prolate group which is directly populated by the heavy-ion induced fusion reactions in the HICOL simulations. However, it is not clear whether this bottleneck exists in reality. One can change from a prolate to an oblate deformation without passing through sphericity, as we are forced to with only the spheroidal degree of freedom. Whether diffusion along triaxial degrees of freedom is fast enough to equilibrate the entire shape degrees of freedom before evaporation occurs remains to be seen. For heavier systems, such as the ^{160}Yb, no similar angular-momentum window is predicted as the bottleneck occurs at larger spins where the fission barrier is very small.

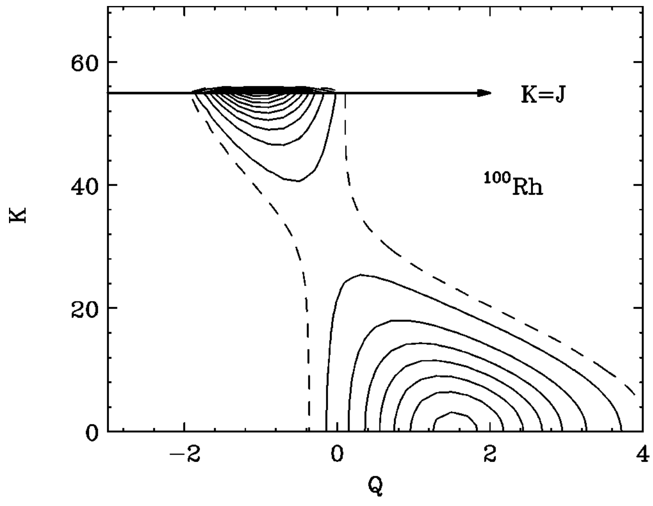

FIG. 18. As for Fig. 2(a), but now for the $J=55\hbar$, $E^*=100$ MeV ^{100}Rh system.

Apart from this angular-momentum window discussed above, nonequilibrium collective effects are predicted to occur at approximately a constant excitation energy with little dependence on spin. As such, they might well be observed from the evolution of the α-particle spectra with bombarding energy. The exact value at which these effects first occur is dependent on the magnitude of the dissipation. If the wall formula significantly overestimates nuclear dissipation as suggested by Griffin and Dworzecka [51], both τ_{dyn} and τ_c will be smaller and E_c^* will be larger. Experimental studies of the entrance-channel dependence of statistical GDR gamma and charge α-particle emission [52,18] have suggested the dissipation is even larger, which would imply the value of E_c^* is smaller. Experimental determination of E_c^* should permit the magnitude of the dissipation to be deduced.

The time scale for the equilibrium of the shape degrees of freedom is strongly related to the predictions of transient fission decay widths. The equilibrium fission decay rate used in statistical-model codes is applicable only after the distribution of shapes has equilibrated. A number of theoretical studies [53–55] have followed the diffusion probability current over the fission barrier when the initial distribution is concentrated near the minimum in the potential-energy surface. Not surprisingly, due to the initial condition, these studies find the fission rate is initially suppressed approaching the equilibrium fission rate only at larger times. This predicted behavior has given rise to the concept of a fission delay which may be important in explaining the large fission time scales measured experimentally [56]. The standard equilibrium decay rates are valid for B_f (fission barrier) $\gg T$, and in such cases the saddle-point deformation is large compared to the typical shapes described by the equilibrium distributions for which $V(Q) \lesssim T$. As longer diffusion times will be required to populate the larger deformations, for the assumed initial condition the fission delay time should be longer than τ_c. However, given the rapid build up of the fluctuations compared to the dynamics of the mean deformation in the Langevin simulations, it is not clear that the assumed initial condition is appropriate for all reactions. For more symmetric fusion reactions, the initial condition consistent with the previous discussions is a large deformation possibility closer to the saddle-point configuration rather than the minimum in the potential-energy surface. In such a scenario, the fluctuations may lead to transient fission enhancements.

VI. COMPARISON TO EXPERIMENT

In this section, calculated multichance kinetic-energy spectra will be compared to experimental data measured in

TABLE I. Experimental data used in comparison with statistical-model calculations. The compound nucleus CN, bombarding energy $E_{\rm beam}$, excitation energy E^*, and measured and predicted α multiplicities m_α are listed. Predicted multiplicities m_α (GEM) were obtained with standard statistical-model calculations and with calculations that consider the equilibrium distributions of compound-nucleus shapes. The level-density parameter a used in each of the calculations is indicated.

Reaction	CN	$E_{\rm beam}$ (MeV)	E^* (MeV)	a (MeV^{-1})	m_α (exp)	m_α (GEM) (shape dist.)	m_α (GEM) (standard)	Reference
^{12}C+^{144}Sm	^{156}Er	142	113	$A/8$	0.7±0.1	0.53	0.39	[12]
^{64}Ni+^{100}Mo	^{164}Yb	320	101	$A/10$	0.45±0.05	0.60	0.42	[11]
		433	171	$A/10$	0.95±0.10	1.09	0.91	
		576	257	$A/10$	1.6±0.16	1.52	1.36	
		640	297	$A/10$	2.1±0.21	1.81	1.64	
^{20}Ne+^{150}Nd	^{170}Yb	270	135	$A/10$				[6]
^{28}Si+^{165}Ho	^{193}Tl	145	65	$A/10$	0.11±0.04	0.10	0.08	[10]
		166	83	$A/10$	0.30±0.12	0.29	0.20	
		193	106	$A/10$	0.59±0.24	0.53	0.41	
		216	126	$A/10$	0.69±0.28	0.72	0.58	
^{16}O+^{197}Au	^{213}Fr	114	74	$A/11$	0.17±0.07	0.35	0.22	[10]
		138	98	$A/11$	0.46±0.18	0.70	0.51	
^{16}O+^{208}Pb	^{224}Th	114	61	$A/13$	0.22±0.09	0.16	0.08	[10]
		138	84	$A/13$	0.56±0.22	0.34	0.18	

coincidence with evaporation residues. In the GEMINI Monte Carlo simulations, values of Q and K are chosen from the appropriate equilibrium distributions at each step in the evaporation cascade. Otherwise, the values of Q and K at different steps are assumed to be uncorrelated. At each step, an evaporated particle and its kinetic energy are selected in a Monte Carlo fashion from the probabilities calculated with the chosen values of Q and K. α-particle kinetic-energy spectra were constructed from all α particles emitted in evaporation cascades that produce evaporation residues. When making comparisons to experimental data, it is important to remember the limitations of these calculations. First, the approximate nature of the method used to calculate the transmission coefficients has already been stressed in Sec. III B. Even if more accurate transmission coefficients are available, only the spheroidal shape degree of freedom has been considered in these calculations. When ellipsoidal shapes are allowed, the Coulomb-barrier distribution is additionally enhanced for low-energy barriers; this would further increase the yield in the ‘‘sub-barrier’’ region [33]. In spite of these limitations, it is useful to determine whether these present calculations predict a sub-barrier enhancement of the right order and whether extra enhancements are required at higher excitation energies indicating that collective pre-equilibrium effects are at play.

It was decided to restrict the comparison to experimental data with $A>150$. For lighter systems, the neck degree of freedom is of increasing importance at the saddle-point configuration [38] and the simple spheroidal shape parametrization, which lacks this degree of freedom, is probably inadequate for the larger prolate-like deformations. Also due to the angular-momentum dependence of the predicted sub-barrier enhancement, it was decided to restrict comparison to α-particle spectra (residue gated) where also the evaporation residue cross sections have been measured. The experimental evaporation-residue cross sections allow one to restrict the range of compound-nucleus spins contributing to α-particle emission. With these considerations, data from the reactions listed in Table I were selected for comparison. In all cases, except the C+Sm reaction, l waves contributing to residue production are limited by fission competition at the higher spins. The statistical fission parameters needed to fit the residue cross sections were taken from the values fitted by the authors of the studies referenced in Table I. These parameters also allowed adequate reproduction of the measured cross sections in the present calculations. Also included in Table I is the Ne+Nd reaction of Ref. [6] for which the α-particle spectra are gated on high gamma-ray multiplicities selected to remove contributions from other reaction mechanisms besides fusion evaporation. The fission parameters in this case were taken from the Ni+Mo reaction [11], which produces a very similar compound nucleus. For the C+Sm reaction, the measured residue cross section was used to restrict the fusion l-wave distribution in the same manner as in Ref. [12].

Level-density parameters were varied from $A/8$ to $A/13$ MeV^{-1} with increasing A (see Table I) to approximately reproduce the high-energy slopes of experimental α-particle spectra. This dependence is itself interesting and may be an artifact of using a temperature-independent level-density parameter. Better reproduction of the slopes of the spectra at high energies could be obtained with temperature-dependent level-density parameters [10], however it was decided not to introduce such an effect at present so as not to add confusion as to the importance of the different modifications, but to concentrate on reproducing the subbarrier region. For all of the experimental data sets studied, the authors were unable to reproduce the experimental α-particle

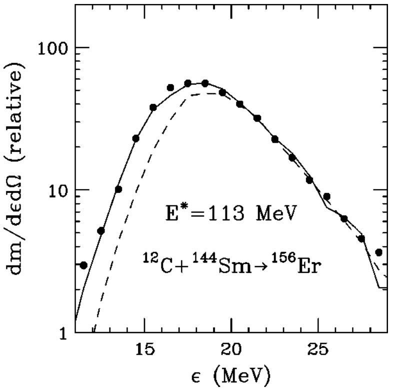

FIG. 19. Comparison of experimental and predicted α-particle kinetic-energy spectra in coincidence with evaporation residues produced in the $^{12}C+^{144}Sm$ reaction (see Table I). The prediction, indicated by the solid curve, was obtained including the equilibrium shape distributions at each step of the decay. The dashed curve is a more standard prediction using spherical transmission coefficients. The excitation energy of the compound nucleus is indicated.

spectra in the sub-barrier region with standard statistical-model calculations using spherical transmission coefficients (even with temperature-dependent level-density parameters).

The predicted α-particle multiplicities are compared to experimental values in Table I and the predicted shapes of energy spectra (solid curves) are compared to the experimental data in Figs. 19–24. The predicted spectra have been normalized to give the same maximum yield as the experimental data to focus our attention on the differences in the shapes of these spectra. To show the magnitude of the sub-barrier enhancements, more standard calculations using spherical transmission coefficients and Sierk's rotational energies were performed and the results are also listed in Table I and are indicated by the dashed curves in the figures. The predicted multiplicities are in good agreement with the experimental values. The calculations including the equilibrium distributions of shapes predict higher multiplicities and, overall, are in better agreement with the data, but the sensitivity of the multiplicities to the nuclear shape is not that great. However, the largest difference between the two calculations is the sub-barrier enhancement that is produced when the equilibrium distribution of shapes is included. The magnitude of this enhancement can be gauged by the differences between the solid and dashed curves.

First, let us focus our attention on reactions with asymmetric entrance channels ($A_{\mathrm{proj}}<20$) shown in Figs. 19–23. The compound-nucleus excitation energies for these systems are 135 MeV or less and the calculations reproduced the experimental data exceedingly well. Although the extent of this agreement may be somewhat fortuitous, given the limitations discussed above, the magnitude of the sub-barrier enhancement is of the right order. In addition, the spectra gated on gamma-ray multiplicity in Fig. 20 confirm the predicted increase of this enhancement with increasing spin. In this figure, the experimental spectra gated on low ($k_\gamma=11$–14) and high ($k_\gamma=27$–33) gamma-ray multiplicities are plotted. The detected multiplicity is related to the spin of the residue J_r after the termination of the particle evaporation cascade. To compare with experimental data, we have used the relationship $\langle k_\gamma\rangle=J_r/2+5.3$ [57] to gate the statistical-model predictions. The predicted increase in the sub-barrier enhancement with spin is again correctly reproduced.

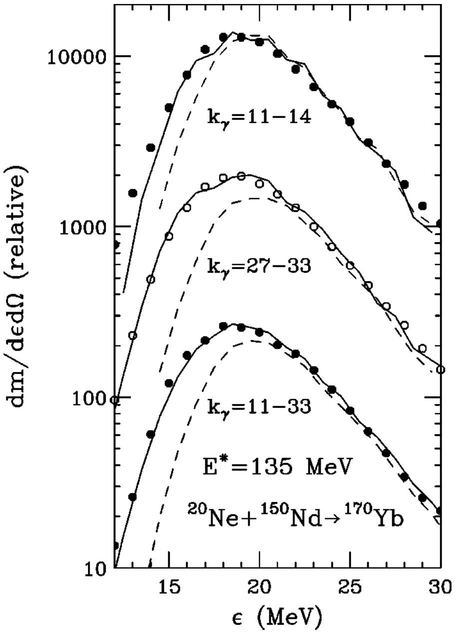

FIG. 20. Same as for Fig. 19, but now the data are from the $^{20}Ne+^{150}Nd$ reaction and the spectra are gated on the measured gamma-ray multiplicity (k_γ). The relative normalization of the different k_γ-gated spectra is arbitrary.

These comparisons with the experimental data give no indication for the need of any extra sub-barrier enhancement associated with collective nonequilibrium emissions at the highest excitation energies. To look for such effects it is

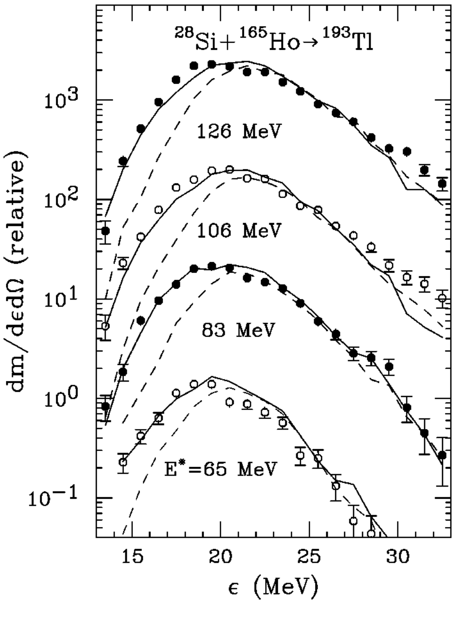

FIG. 21. As for Fig. 19, but now the data are from the $^{28}Si+^{165}Ho$ reaction. The relative normalization of the spectra at different excitation energies is arbitrary.

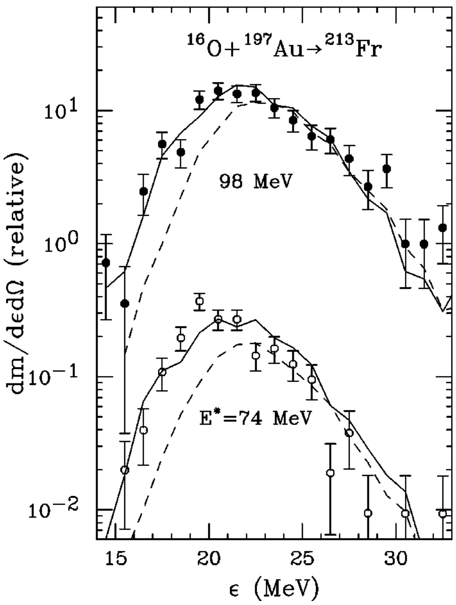

FIG. 22. As for Fig. 19, but now the data are from the ^{16}O $+{}^{197}$Au reaction. The relative normalization of the spectra at different excitation energies is arbitrary.

useful to examine more asymmetric entrance channels and higher excitation energies where these effects should be larger. The data from the Ni+Mo reaction in Fig. 24 are most suitable in this regard as it covers the largest range of excitation energies. At the lowest excitation energy (101 MeV), the predicted enhancement of sub-barrier α particles is again of the right order. However, for the higher excitation energies, substantially larger enhancements are needed to reproduce the data. Some of this extra enhancement will come from the decay of evaporated ^{5}He and other unstable clusters. However, in the $E/A=11$ MeV ^{60}Ni$+{}^{100}$Mo reaction ($E^*=300$ MeV), this component is only dominant for α-particle kinetic energies below 10 MeV and cannot explain the yield near the peak of the spectra [13]. Possibly, the inclusion of other shape degrees of freedom which are excited at high excitation energies may contribute to a further enhancement. However, from the discussion in Sec. V, it would not seem unreasonable that for excitation energies of 170 MeV and larger, some evaporation occurs before the shape degrees of freedom are fully equilibrated. The HICOL simulations for large l-waves populate the prolate $K=0$ minima [Fig. 2(b)] and thus it is expected that the preequilibrium shape distributions will be weighted towards these prolate shapes which are responsible for most of the sub-barrier enhancement (Sec. IV B). Thus, the increased experimental enhancement at the larger excitation energies is qualitatively consistent with collective preequilibrium evaporation. Some confirmation of this suggestion comes from a comparison of the O+Sm and Ni+Mo reactions in Ref. [11] which were matched to 170 MeV of excitation energy. The measured residue-gated α-particle spectra from these reactions both show some extra sub-barrier enhancement compared to the present calculations. However, this enhancement is larger for the Ni+Mo reaction, consistent with the HICOL predictions of larger initial prolate deformations for the more symmetric entrance channel.

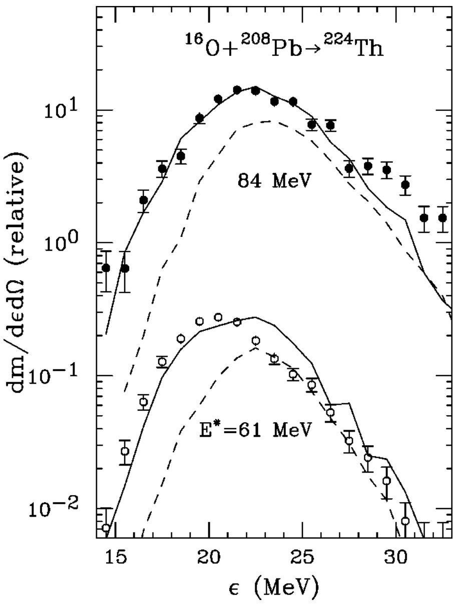

FIG. 23. As for Fig. 19, but now the data are from the ^{16}O $+{}^{208}$Pb reaction. The relative normalization of the spectra at different excitation energies is arbitrary.

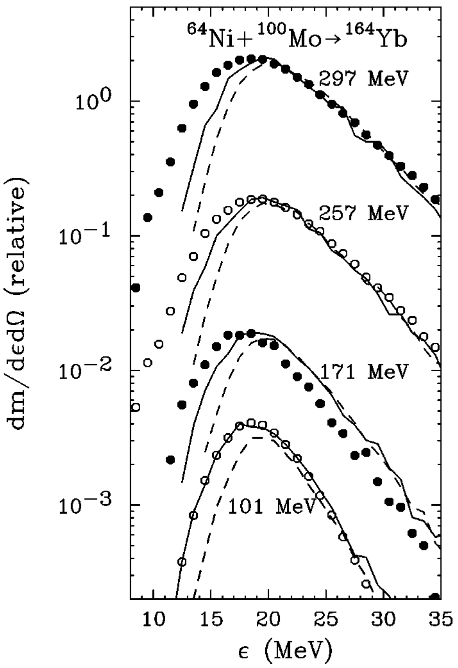

FIG. 24. As for Fig. 19, but now the data are from the ^{64}Ni $+{}^{100}$Mo reaction. The relative normalization of the spectra at different excitation energies is arbitrary.

Liang *et al.* [12] have interpreted an entrance-channel dependence of the hardness of experimental proton and α-particle spectra as evidence for collective preequilibrium emissions. The reactions studied were ^{12}C$+{}^{144}$Sm and ^{60}Ni $+{}^{96}$Zr making the same compound nucleus with 113 MeV of excitation energy and similar spin distributions. More symmetric entrance channels have larger initial deformations in the HICOL simulations and thus are expected to have lower initial thermal excitation energies. The initially cooler Ni + Zr compound system is thus expected to have softer spectra, as observed. The magnitude of this effect is consistent with HICOL simulations [12]. However, the possibility of significant nucleonic preequilibrium emission (at large angles) for the C + Sm reaction could also account for the observed differences. As further support for this latter interpretation, the sub-barrier region of the experimental α-particle spectra shows no significant entrance-channel dependence and is well accounted for in the present calculations (Fig. 19). This is unlike the results for the higher excitation energy O + Sm and Ni + Mo reactions discussed above.

Clearly, more systematic experimental studies of the evolution of α-particle spectra with excitation energy and entrance-channel asymmetry are called for. In addition to this, it is important to obtain theoretical estimates for the magnitude of the extra sub-barrier enhancement associated with collective preequilibrium emissions. This task could be accomplished by adding evaporation to Langevin simulations similar to those discussed in this work. It is also of interest to determine the excitation-energy dependence of this extra enhancement which is not clear at present. Although the amount of collective preequilibrium α-particle emission should increase with excitation energy, the initial fusion deformation decreases with increasing bombarding energy in the HICOL simulations. A better understanding of the evolution of α-particle spectra with excitation energy might allow the strength of nuclear dissipation to be deduced.

As already mentioned, the inclusion of the equilibrium shape distribution has little effect on the predicted proton and neutron spectra. Within the statistics of the GEMINI Monte Carlo simulations, it is difficult to discern any difference between the neutron spectra calculated with and without the inclusion of the equilibrium shape distributions and only minor differences were obtained for protons. Therefore, all conclusions made in Refs. [10–12] concerning the experimental proton spectra for the reactions in Table I still hold. In some cases a modest enhancement of the sub-barrier protons would improve agreement with the experimental data. However, given the insensitivity of the calculations to deformation, the explanation of this effect would seem to lie elsewhere.

For all but the two heaviest compound systems (^{16}O + ^{197}Au and ^{16}O + ^{208}Pb reactions) the evaporation residues are predicted to lie close to the evaporation attractor line [58] at which proton and neutron decay rates are similar at all excitation energies. In the GEMINI simulations for these systems, low-energy ''sub-barrier'' protons are mostly last-chance evaporation and thus shell and structure effects may be important in explaining their yields. For the heavy systems, the residues are more neutron rich compared to the attractor line and at low excitation energies practically only neutrons are evaporated. Consequently, almost all protons are evaporated early in the decay cascade. Shell and structure effects should be less important for these systems and good agreement between the experimental and calculated proton spectra is obtained [10].

VII. CONCLUSION

Thermal fluctuations give rise to an equilibrium distribution of compound-nucleus shapes and spin projections. A full understanding of the evaporative decay probabilities of compound nuclei requires a knowledge of how these quantities affect the statistical decay width. In this work, the equilibrium distributions have been determined for spheroidal shaped nuclei. Both prolate and oblate shapes are populated, but at high spins the overall nature of the distribution is somewhat more prolate with the tail of the distribution extending out to very deformed (axis ratio of 2:1) shapes even for moderate excitation energies. The Hauser-Feshbach formalism has been extended to describe the dependence of the decay width on the quadrupole deformation and the spin projection K. In general, deformation increases the probability for α-particle emission; the exact extent depends on the value of K. When averaged over the equilibrium distributions, the increased α-particle probability is preferentially for low kinetic energies, enhancing the ''sub-barrier'' region compared to standard calculations using spherical transmission coefficients. The effect on predicted neutron and proton kinetic-energy spectra is much smaller. The magnitude of the sub-barrier α-particle enhancement is larger for high-spin systems, the largest contribution coming from highly deformed prolate shapes.

In general, as the excitation energy increases, one should observe collective preequilibrium effects associated with evaporation before the distributions of shape and spin projection have thermalized. The time scale for thermalization has been explored with Langevin simulations, using the dissipation strength predicted by the wall formula of Ref. [50]. From these simulations, the shape and spin-projection distributions will become thermalized before significant evaporation occurs if the excitation energy is ~100 MeV or less. However, if the dissipation strength is smaller, then this maximum excitation energy will be larger. At higher excitation energies, collective preequilibrium emission will occur until the system cools down below this maximum excitation energy. Based on the predictions of the dynamical code HICOL [49], we expect the preequilibrium shape distribution to emphasize large prolate shapes for heavy-ion induced fusion reactions and this will further increase the predicted enhancement of sub-barrier α particles.

A preliminary comparison of predicted α-particle kinetic-energy spectra with experimental data from asymmetric collisions with excitation energies less than 135 MeV indicates that the inclusion of the equilibrium shape distributions produces a sub-barrier α-particle enhancement of the correct order. Data from more symmetric entrance channels give indications that collective preequilibrium α-particle emission is occurring at excitation energies above 100 MeV, however a quantitative understanding of these data is not available at present. Further experimental and theoretical studies are needed and these may allow the strength of nuclear dissipation to be deduced.

ACKNOWLEDGMENTS

I wish to acknowledge many informative discussions with Professor Lee Sobotka and Professor Ron Lovett. I would also like to thank Dr. Felix Liang and Dr. Brian Fineman for providing me with their data. This work was supported by the Director, Office of High Energy and Nuclear Physics, Nuclear Physics Division of the U.S. Department of Energy under Contract No. DE-FG02-87ER-40316.

---

[1] V.F. Weisshopf and D.H. Ewing, Phys. Rev. **57**, 472 (1940).
[2] W. Hauser and H. Feshbach, Phys. Rev. **87**, 366 (1952).
[3] G. La Rana, D.J. Moses, W.E. Parker, M. Kaplan, D. Logan, R. Lacey, J.M. Alexander, and R.J. Welberry, Phys. Rev. C **35**, 373 (1987).
[4] R. Lacey, N.N. Ajitanand, J.M. Alexander, D.M. de Castro Rizzo, P. Deyoung, M. Kaplan, L. Kowalski, G. La Rana, D. Logan, D.J. Moses, W.E. Parker, G.F. Peaslee, and L.C. Vaz, Phys. Lett. B **191**, 253 (1987).
[5] G. La Rana, R. Moro, A. Brondi, P. Cuzzocrea, A. D'Onofrio, E. Perillo, M. Romano, F. Terrasi, E. Vardaci, and H. Dumont, Phys. Rev. C **37**, 1920 (1988).
[6] N.G. Nicolis, D.G. Sarantites, L.A. Adler, F.A. Dilmanian, K. Honkanen, Z. Majka, L.G. Sobotka, Z. Li, T.M. Semkow, J.R. Beene, M.L. Halbert, D.C. Hensley, J.B. Natowitz, R.P. Schmitt, D. Fabris, G. Nebbia, and G. Mouchaty, Phys. Rev. C **41**, 2118 (1990).
[7] M. Gonin, L. Cooke, K. Hagel, Y. Lou, J.B. Natowitz, R.P. Schmitt, S. Shlomo, B. Srivastava, W. Turmel, H. Utsunomiya, R. Wada, G. Nardelli, G. Nebbia, G. Viesti, R. Zanon, B. Fornal, G. Prete, K. Niita, S. Hannuschke, P. Gonthier, and B. Wilkins, Phys. Rev. C **42**, 2125 (1990).
[8] M. Kildir, G. La Rana, R. Moro, A. Brondi, A. D'Onofrio, E. Perillo, V. Roca, M. Romano, F. Terrasi, G. Nebbia, G. Viesti, and G. Prete, Phys. Rev. C **46**, 2264 (1992).
[9] J. Boger, J.M. Alexander, R.A. Lacey, and A. Narayanan, Phys. Rev. C **49**, 1587 (1994).
[10] B.J. Fineman, K.-T. Brinkmann, A.L. Caraley, N. Gan, R.L. McGrath, and J. Velkovska, Phys. Rev. C **50**, 1991 (1994).
[11] R.J. Charity, M. Korolija, D.G. Sarantites, and L.G. Sobotka, Phys. Rev. C **56**, 873 (1997).
[12] J.F. Liang, J.D. Bierman, M.P. Kelly, A.A. Sonzogni, R. Vandenbosch, and J.P.S. van Schagan, Phys. Rev. C **56**, 908 (1997).
[13] R.J. Charity, L.G. Sobotka, J. Cibor, K. Hagel, M. Murray, J.B. Natowitz, R. Wada, Y. El Masri, D. Fabris, G. Nebbia, G. Viesti, M. Cinausero, E. Fioretto, G. Prete, A. Wagner, and H. Xu (unpublished).
[14] J. Galin, B. Gatty, D. Guerreau, U.C. Schlotthauser-Voos, and X. Tarrago, Phys. Rev. C **10**, 638 (1974).
[15] Z. Majka, M.E. Brandan, D. Fabris, K. Hagel, A. Menchaca-Rocha, J.B. Natowitz, G. Nebbia, G. Prete, B. Sterling, and G. Viesti, Phys. Rev. C **35**, 2125 (1987).
[16] J.R. Huizenga, A.N. Behkami, I.M. Govil, W.U. Schröder, and J. Tõke, Phys. Rev. C **40**, 668 (1989).
[17] X.S. Chen, C. Ngô, E. Tomasi, M. Barranco, X. Viñas, and H. Ngô, Nucl. Phys. A **401**, 143 (1983).
[18] M. Korolija, R.J. Charity, N.G. Nicolis, D.G. Sarantites, and L.G. Sobotka, Phys. Rev. C **52**, 3074 (1995).
[19] M. Cabbibbo, V. Baran, M. Colonna, and M. Di Toro, Nucl. Phys. **A637**, 374 (1998).
[20] Y. Alhassid and B. Bush, Phys. Rev. Lett. **65**, 2527 (1990).
[21] W.E. Ormand, P.F. Bortignon, and R.A. Broglia, Phys. Rev. Lett. **77**, 607 (1996).
[22] L.G. Moretto, K.X. Jing, L. Phair, and G.J. Wozniak, J. Phys. G **23**, 1323 (1997).
[23] L.G. Moretto, Nucl. Phys. **A247**, 211 (1975).
[24] R.W. Hasse and W.D. Myers, *Geometric Relationships of Macroscopic Nuclear Physics* (Springer-Verlag, Berlin, 1988).
[25] S. Bjørnholm, A. Bohr, and B.R. Mottelson, *Physics and Chemistry of Fission* (International Atomic Energy Agency, Vienna, 1974), Vol. I, p. 367.
[26] S. Cohen and W.J. Swiatecki, Ann. Phys. (N.Y.) **22**, 406 (1963).
[27] W.D. Myers and W.J. Swiatecki, Nucl. Phys. **81**, 1 (1966).
[28] W.D. Myers and W.J. Swiatecki, Ark. Fys. **36**, 343 (1967).
[29] R. Beringer and W.J. Knox, Phys. Rev. **121**, 1195 (1961).
[30] A.J. Sierk, Phys. Rev. C **33**, 2039 (1986).
[31] S. Cohen, F. Plasil, and W.J. Swiatecki, Ann. Phys. (N.Y.) **82**, 557 (1974).
[32] G. Andersson, S.E. Larsson, G. Leander, P. Möller, S.G. Nilsson, I. Ragnarsson, S. Åberg, R. Bengtsson, J. Dudek, B. Nerlo-Pomorska, K. Pomorski, and Z. Szymański, Nucl. Phys. **A268**, 205 (1976).
[33] R.J. Charity (unpublished).
[34] M. Blann, Phys. Rev. C **21**, 1770 (1980).
[35] N.N. Ajitanand, G. La Rana, R. Lacey, D.J. Moses, L.C. Vaz, G.F. Peaslee, D.M. de Castro Rizzo, M. Kaplan, and J.M. Alexander, Phys. Rev. C **34**, 877 (1986).
[36] V.P. Aleshin, Nucl. Phys. **A605**, 120 (1996).
[37] S.E. Vigdor and H.J. Karwowski, Phys. Rev. C **26**, 1068 (1982).
[38] K.-H. Schmidt, J.G. Keller, and D. Vermeulen, Z. Phys. A **315**, 159 (1984).
[39] J.P. Lestone, J.R. Leigh, J.O. Newton, D.J. Hinde, J.X. Wei, J.X. Chen, S. Elfstrom, and D.G. Popescu, Phys. Rev. Lett. **67**, 1078 (1991).
[40] R.G. Stokstad and E.E. Gross, Phys. Rev. C **23**, 281 (1981).
[41] A. Messiah, *Quantum Mechanics* (Wiley, New York, 1961), Vol. II, p. 1070.
[42] J.M. Alexander, M.T. Magda, and S. Landowne, Phys. Rev. C **42**, 1092 (1990).
[43] D. Wilmore and P.E. Hodgson, Nucl. Phys. **55**, 673 (1964).
[44] F.G. Perey, Phys. Rev. **131**, 745 (1963).
[45] L. McFadden and G.R. Satchler, Nucl. Phys. **84**, 177 (1966).
[46] K. Dietrich, K. Pomorski, and J. Richert, Z. Phys. A **351**, 397 (1995).
[47] R.J. Charity, Computer code GEMINI (unpublished). A Fortran-95 version of this code, containing the modifications

mentioned in the text, is available via anonymous FTP from wunmr.wustl.edu in directory/pub/gemini95.

[48] A.V. Ignatyuk, M.G. Itkis, V.N. Okolovich, G.N. Smirenkin, and A.S. Tishin, Yad. Fiz. **49**, 1185 (1975) [Sov. J. Nucl. Phys. **21**, 612 (1976)].

[49] Computer code HICOL, H. Feldmeier, Prog. Phys. **50**, 915 (1987).

[50] J. Błocki, Y. Boneh, J.R. Nix, J. Randrup, M. Robel, A.J. Sierk, and W.J. Swiatecki, Ann. Phys. (N.Y.) **113**, 330 (1978).

[51] J.J. Griffin and M. Dworzecka, Nucl. Phys. **A455**, 61 (1986).

[52] M. Thoennessen, J.R. Beene, F.E. Bertrand, C. Baktash, M.L. Halbert, D.J. Horen, D.G. Sarantites, W. Spang, and D.W. Stracener, Phys. Rev. Lett. **70**, 4055 (1993).

[53] K.H. Bhatt, P. Grangé, and B. Hiller, Phys. Rev. C **33**, 954 (1986).

[54] P. Grangé, S. Hassani, H.A. Weidenmüller, A. Gavron, J.R. Nix, and A.J. Sierk, Phys. Rev. C **34**, 209 (1986).

[55] D. Boilley, E. Suraud, Y. Abe, and S. Ayik, Nucl. Phys. **A556**, 67 (1993).

[56] D. Hilscher and H. Rossner, Ann. Phys. (Paris) **17**, 471 (1992).

[57] D.G. Sarantites, L. Westerberg, M.L. Halbert, R.A. Dayras, D.C. Hensley, and J.H. Barker, Phys. Rev. C **18**, 774 (1978).

[58] R.J. Charity, Phys. Rev. C **58**, 1073 (1998).